Orcinol glucoside ameliorates pulmonary fibrosis by suppressing hyaluronic acid synthesis and macrophage M2 polarization via targeting hyaluronic acid synthase 2

CAIZI LI[1*], XINGLINZI TANG[1*], XIAORU LUO[1*], XIN LAI[1], JING YANG[1], ZHENG XU[1], GULIZEBA MUHETAER[2], YIZI XIE[3-6], XIUFANG HUANG[3-6] and HANG LI[1]

[1]Central Laboratory, Shenzhen Bao'an Chinese Medicine Hospital, Guangzhou University of Chinese Medicine, Shenzhen, Guangdong 518133, P.R. China; [2]The Second Clinical Medical School, Guangzhou University of Chinese Medicine, Guangzhou, Guangdong 511436, P.R. China; [3]The First Affiliated Hospital of Guangzhou University of Chinese Medicine, Guangzhou, Guangdong 510405, P.R. China; [4]Lingnan Medical Research Center of Guangzhou University of Chinese Medicine, Guangzhou, Guangdong 510405, P.R. China; [5]The First Clinical Medical School, Guangzhou University of Chinese Medicine, Guangzhou, Guangdong 510405, P.R. China; [6]Guangdong Provincial Clinical Research Academy of Chinese Medicine, Guangzhou, Guangdong 510405, P.R. China

Received August 19, 2025; Accepted January 16, 2026

DOI: 10.3892/ijmm.2026.5764

Abstract. Idiopathic pulmonary fibrosis (IPF) is a chronic, progressive lung disorder characterized by unexplained fibrosis and limited therapeutic options, highlighting the urgent need for innovative treatments. Hyaluronic acid (HA), which is upregulated in IPF and correlates with disease severity, plays an undefined role in its pathogenesis. Hyaluronic acid synthase 2 (HAS2), a key enzyme in HA production, has an unclear function in IPF progression, particularly regarding its involvement in macrophage polarization. Understanding this mechanism is essential for identifying novel therapeutic targets and developing effective drugs for IPF. The present study investigated the roles of HAS2 and HA in IPF and identified potential therapeutic agents. Transcriptomic analysis revealed HAS2 as a critical IPF-associated gene in patient samples, bleomycin (BLM)-induced mouse models, and transforming growth factor β1 (TGF-β1)-induced myofibroblasts. Single-cell RNA sequencing further confirmed the fibroblast-specific upregulation of HAS2 in fibrotic lungs. Experimental validation showed elevated HAS2 expression and HA accumulation in fibrosis models. HA facilitated macrophage M2 polarization and TGF-β1 secretion through CD44-dependent STAT6 activation, with CD44 inhibition blocking this effect. Knockdown of HAS2 in fibroblasts decreased HA release and impaired their ability to promote M2 polarization, suggesting that fibroblast-derived HA drives this process. High-throughput virtual screening, coupled with absorption, distribution, metabolism and excretion (ADME) profiling, identified orcinol glucoside (OG) as a potential HAS2 inhibitor, which was validated through surface plasmon resonance, cellular thermal shift assays, and molecular dynamics simulations. OG suppressed HA synthesis in TGF-β1-induced and HAS2-overexpressing myofibroblasts in a dose-dependent manner, inhibiting M2 polarization induction. *In vivo*, OG reduced collagen deposition, HA, and TGF-β1 levels in BLM-induced fibrotic mice. These findings established HAS2 as a central pathogenic factor in IPF and suggested OG as a promising therapeutic candidate, providing a novel approach for IPF treatment by targeting HA synthesis and macrophage polarization.

Correspondence to: Dr Xiufang Huang, Lingnan Medical Research Center of Guangzhou University of Chinese Medicine, Ji Chang Road, Guangzhou, Guangdong 510405, P.R. China
E-mail: huangxf28@foxmail.com

Professor Hang Li, Central Laboratory, Shenzhen Bao'an Chinese Medicine Hospital, Guangzhou University of Chinese Medicine, 25 Yu'an Second Road, Shenzhen, Guangdong 518133, P.R. China
E-mail: lihang@gzucm.edu.cn

*Contributed equally

Key words: idiopathic pulmonary fibrosis, hyaluronic acid synthase 2, hyaluronic acid, orcinol glucoside, macrophage

Introduction

Idiopathic pulmonary fibrosis (IPF) is a progressive interstitial lung disease characterized by irreversible scarring of lung tissue, posing a severe threat to middle-aged and elderly populations globally. With a median survival of only 3-5 years post-diagnosis, IPF presents a clinical challenge, offering few effective treatment options (1,2). Although treatments like pirfenidone and nintedanib can slow disease progression, they do not provide a cure (3). This limitation highlights the urgent need for the discovery of new molecular targets and effective

pharmacological strategies to halt or reverse the progression of IPF.

The pathogenesis of IPF is driven by abnormal extracellular matrix (ECM) accumulation, primarily regulated by the transformation of fibroblasts into myofibroblasts. These myofibroblasts excessively produce collagen and ECM proteins, leading to gradual lung damage (4). Among ECM components, hyaluronic acid (hyaluronan, HA), a prominent glycosaminoglycan, plays a pivotal role in regulating cellular processes such as proliferation, migration and differentiation (5,6). Clinical studies have shown that HA is a critical factor in IPF: HA concentrations are markedly elevated in the bronchoalveolar lavage fluid of patients with IPF compared with healthy controls (7,8). Furthermore, HA levels correlate inversely with lung function and are higher in patients with progressive disease, linking HA to disease severity and progression (7).

HA production is mediated by the hyaluronic acid synthase (HAS) family, which includes three isoforms (HAS1, HAS2 and HAS3), using uridine diphosphate glucuronic acid (UDP-GlcA) and uridine diphosphate N-acetylglucosamine (UDP-GlcNAc) as substrates (9,10). Of these, HAS2 is the most abundant and functionally significant variant, responsible for synthesizing HA and controlling its distribution in tissues (11). Given the elevated levels of HA in IPF and the central role of HAS2 in HA production, investigating the HAS2-HA pathway has emerged as a promising avenue for understanding the mechanisms underlying IPF.

A significant knowledge gap exists in delineating the specific roles of HAS2 and HA in the development of IPF. While elevated HA levels are well-documented, the mechanistic links between HAS2-driven HA production and key pathological processes in IPF remain underexplored. Notably, macrophage polarization, especially the shift toward the pro-fibrotic M2 subtype, is a major contributor to IPF pathogenesis (12). However, the effect of HAS2 and HA on this polarization process is not fully understood. Moreover, despite the potential of HAS2 as a therapeutic target, no effective interventions specifically targeting HAS2 have been developed, leaving a critical gap in IPF treatment options.

The present study aimed to address these critical gaps by investigating the role of HAS2 in the development of IPF and evaluating the therapeutic potential of targeting HAS2 to mitigate pulmonary fibrosis. Specifically, it was hypothesized that HAS2-driven HA production exacerbated IPF progression by enhancing myofibroblast activity and promoting macrophage M2 polarization. To test this hypothesis, the present study employed a multidisciplinary approach, combining *in vitro* cell models, *in vivo* disease models, transcriptomic analysis and high-throughput virtual screening. The primary objectives included: Defining the mechanistic interactions between HAS2, HA and macrophage M2 polarization in IPF; elucidating the effects of HAS2 inhibition on ECM deposition and fibroblast activation; and assessing the therapeutic potential of novel HAS2-targeting compounds in reducing pulmonary fibrosis.

Materials and methods

Cell culture. The NIH/3T3 mouse embryo fibroblast, HFL-1 human fetal lung fibroblast and RAW264.7 mouse monocyte macrophage leukemia cell lines were obtained from the National Collection of Authenticated Cell Cultures. NIH/3T3 and RAW264.7 cells were cultured in complete DMEM (Gibco; Thermo Fisher Scientific, Inc.), while HFL-1 cells were maintained in complete Ham's F-12K medium (Procell Life Science & Technology Co., Ltd.). All media were supplemented with 10% fetal bovine serum and 1% penicillin-streptomycin (Gibco; Thermo Fisher Scientific, Inc.). The cultures were incubated at 37˚C with 5% CO_2.

Mining differential expression genes in IPF lungs from the gene expression omnibus (GEO) database. A comprehensive analysis was performed using the GEO database (13) to explore gene expression differences between normal and IPF-affected lung tissues. The focus was on the GSE110147 dataset, which includes expression profiles from 11 normal lung tissue samples (age 52±18 years; Male/Female 7/4) and 22 samples from patients with IPF (age 62±6 years; Male/Female 14/5). Detailed patient information can be found in the referenced literature (14). Differential expression analysis was performed using GEO2R (13) to compare gene expression across sample groups. A significance threshold was set with a Log_2 fold change of 1 and a P-value of 0.05. The Benjamini and Hochberg method was applied to adjust P-values for multiple comparisons, controlling the false discovery rate. A volcano plot was generated using the bioinformatics cloud platform (https://www.bioinformatics.com.cn) for data visualization.

Transcriptome sequencing. For *in vitro* studies, NIH/3T3 fibroblasts were treated with or without 5 ng/ml recombinant TGF-β1 (R&D Systems, Inc.) for 12 h prior to RNA collection for transcriptomic analysis (n=3 per group). Transcriptomic data for these samples were derived from our prior study (15) and were re-analyzed in the context of the present work. For *in vivo* studies, a total of six specific pathogen-free (SPF) male C57BL/6J mice (aged 6-8 weeks, weight 22-24 g) were used. Mice were purchased from Guangdong Vital River Laboratory Animal Technology Co., Ltd. and housed in the SPF-grade animal facility at the Shenzhen Institute of Technology, Hong Kong Polytechnic University. Housing conditions were maintained at a temperature of 22±2˚C, a 12-h light/dark cycle and a humidity of 50±10%. Mice were randomly assigned to either a control group or a bleomycin (BLM)-induced fibrosis model group. After anesthesia with 3-4% isoflurane, pulmonary fibrosis was induced in the model group by intratracheal administration of 2.5 mg/kg BLM (Shanghai Macklin Biochemical Technology Co., Ltd.), while control mice received an equivalent volume of sterile saline. Three weeks post-treatment, lung tissues were harvested for transcriptomic analysis (n=3 per group). Transcriptome sequencing was conducted by Wekemo Tech Group using the Illumina platform (Illumina, Inc.). Gene expression levels were quantified in Fragments Per Kilobase of transcript per Million mapped reads and differential expression analysis was performed using the DESeq2 R package v1.26.0 (16). Genes were considered differentially expressed if their adjusted P-values were <0.05 and Log_2 fold change >1.

Single-cell RNA sequencing. SPF male C57BL/6J mice were randomly assigned to either a control group (saline; n=3) or a pulmonary fibrosis model group (BLM

2.5 mg/kg intratracheal; n=3). Lungs were harvested 14 days post-exposure, preserved in sCelLive solution (Singleron Biotechnologies GmbH), minced, and digested with sCelLive dissociation solution using the PythoN™ System (Singleron Biotechnologies GmbH). Cell suspensions were filtered through a 40 μm mesh, red blood cells were lysed using GEXSCOPE RCLB (Singleron Biotechnologies GmbH), and cell viability was assessed via Trypan Blue staining (Bio-Rad Laboratories, Inc.) at room temperature for 2-3 min. Single-cell suspensions ($2x10^5$ cells/ml) were processed on the Matrix System (Singleron Biotechnologies GmbH) for barcoding, reverse transcription, cDNA amplification, and library construction using GEXSCOPE Kits (Singleron Biotechnologies GmbH). Libraries (4 nM) were sequenced on an Illumina NovaSeq 6000 (150 bp PE; Illumina, Inc.). Raw reads were trimmed using Cutadapt v1.17 (17), aligned to GRCm38 with STAR v2.6.1a (18), and Unique Molecular Identifier (UMI)/gene counts were generated using featureCounts v2.0.1 (19). Using Scanpy v1.8.2 (20), cells were filtered based on gene count (<200 or top 2%), UMI count (top 2%) and mitochondrial content (>50%); genes detected in fewer than 5 cells were excluded, resulting in 76,995 cells retained for analysis. Potential doublets were identified and filtered using Scrublet v0.2.3 (21). Counts were normalized, log-transformed, and the top 2000 variable genes were subjected to Principal Component Analysis. Louvain clustering (resolution=1.2, 32 clusters) using the top 20 PCs was visualized via Uniform Manifold Approximation and Projection (UMAP). Differentially expressed genes (DEGs) were identified with Seurat's (v3.2.3) FindMarkers (22) using the Wilcoxon test (expressed in >10% of cluster cells, mean logFC >0.25). Clusters were annotated using canonical markers (DEGs/literature) and heatmaps. Cell types were assigned via the SynEcoSys database (www.synecosys.com).

Western blotting. Total proteins were isolated from cells or tissue samples using PIPA lysis buffer (Thermo Fisher Scientific, Inc.). Protein concentration was determined using the Pierce BCA Protein Assay Kit (Thermo Fisher Scientific, Inc.) according to the manufacturer's instructions. Equal amounts of protein (20 μg per lane) were separated by SDS-PAGE [Shenzhen Dakewe Bio-engineering Co., Ltd.; cat. no. 8012011; suitable for the separation and identification of (10~250) kDa proteins, without the need to adjust the separation gel concentration based on protein size]. Proteins were then transferred onto PVDF membranes (MilliporeSigma). After blocking for 60 min at room temperature with 5% non-fat milk, the membranes were incubated overnight at 4˚C with primary antibodies. Antibodies for Collagen type I α 1 chain (COL1A1; cat. no. 72026; 1:1,000), Phospho-STAT6 (Tyr641; cat. no. 56554S; 1:1,000) and α-smooth muscle actin (α-SMA; cat. no. 19245; 1:1,000) were obtained from Cell Signaling Technology, Inc. The HAS2 (cat. no. bs-11290R; 1:1,000) antibody was purchased from BIOSS and HRP-conjugated β-tubulin (cat. no. HRP-66240: 1:20,000) and STAT6 (cat. no. 51073-1-AP; 1:5,000) antibodies were obtained from Proteintech Group, Inc. Membranes were incubated for 1 h at room temperature with an HRP-conjugated secondary antibody (Cell Signaling Technology, Inc.; 1:2,000) following TBS-T (containing 0.05% Tween-20) washing. Protein bands were detected using Immobilon Western Chemiluminescent substrate (MilliporeSigma) and imaged with a Tanon 5200 Multi automatic chemiluminescence system (Tanon Science and Technology Co., Ltd.).

Reverse transcription-quantitative (RT-q) PCR. RNA extraction, cDNA synthesis and qPCR were performed according to the manufacturers' protocols. Total RNA was extracted from cells ($1-2x10^6$) or tissue samples using the RNA extraction kit (Accurate Biology). RNA was then reverse transcribed into cDNA using the First-Strand cDNA synthesis kit (TransGen Biotech Co., Ltd.). The SYBR Green Premix qPCR Kit (Accurate Biology) was used to set up the real-time PCR system, and analysis was performed on the Roche LightCycler 480 II (Roche Diagnostics, Ltd.). The thermal cycling conditions were as follows: Initial denaturation at 95˚C for 30 sec; followed by 40 cycles of denaturation at 95˚C for 5 sec, annealing/extension at 60˚C for 30 sec. Data were analyzed using the $2^{-\Delta\Delta Cq}$ method for relative quantification (23), with normalization to GAPDH mRNA levels. Primer sequences for the target genes are provided in Table SI.

Enzyme-linked immunosorbent assay (ELISA). Cell culture supernatants and mouse serum were collected and analyzed using ELISA assay kits according to the manufacturer's instructions. HA content was measured with the HA ELISA kit (Beijing Solarbio Science & Technology Co., Ltd.; cat. no. SEKH-0509), while TGF-β1 levels were assessed using the Mouse TGF-β1 ELISA Kit (Proteintech Group, Inc.; cat. no. KE10005).

Isolation and culture of primary mouse lung fibroblasts. Primary lung fibroblasts were isolated from C57BL/6J mice in both the control (saline-treated) and BLM-induced fibrosis model groups, following an established protocol with minor modifications (24). Briefly, lung tissues were aseptically collected, minced, and subjected to sequential enzymatic digestion with a collagenase/dispase cocktail (1 mg/ml) followed by 0.25% Trypsin-EDTA. After RBC lysis, the cell suspension was resuspended in fibroblast growth medium (DMEM with 10% FBS, 1% penicillin/streptomycin, and amphotericin B) and plated. Explanted tissue fragments were retained in the culture dish to facilitate fibroblast outgrowth. Cells were maintained in a humidified incubator at 37˚C with 5% CO_2 and passaged once they reached confluence. Fibroblasts at passage 2 were harvested for protein analysis.

Flow cytometry analysis. HA was purchased from Shanghai Macklin Biochemical Technology Co., Ltd. To generate low molecular weight HA, the HA sample was subjected to sonication (60 W, 20 sec each time, a total of 3 times) while kept on ice. The molecular size of the HA after sonication was assessed by agarose gel electrophoresis as previously described (25). Briefly, samples alongside HA molecular weight standards (10-200, 400-800, 1,500-2,500 kDa) were separated on a 1% agarose gel, followed by staining with StainsAll (MilliporeSigma) at room temperature with gentle agitation overnight for visualization. To assess macrophage polarization into M1 and M2 subtypes, RAW264.7 macrophages were stimulated with HA *in vitro*. After stimulation for the indicated

time period, RAW264.7 cells (1-5x10^6) were stained with fluorophore-conjugated antibodies targeting canonical surface markers: Phycoerythrin (PE)-labeled anti-CD86 (M1 marker; BioLegend, Inc.; cat. no. 159204) and fluorescein isothiocyanate (FITC)-labeled anti-CD206 (M2 marker; BioLegend, Inc.; cat. no. 141704). Cells were incubated with antibodies in the dark on ice for 30 min, washed twice with cold PBS, and analyzed using a Beckman CytoFlex flow cytometer (Beckman Coulter, Inc.). FlowJo v10 software (BD Biosciences) was used to calculate the percentage of $CD86^+/CD206^+$ subpopulations and quantify phenotypic shifts.

Overexpression and knockdown of HAS2 in fibroblasts. To investigate the functional role of HAS2, the present study employed both gain-of-function and loss-of-function approaches in NIH/3T3 fibroblasts. The lentivirus for overexpression and the shRNA plasmid for knockdown were both designed, constructed and provided by Shanghai GeneChem Co., Ltd. For HAS2 overexpression, a lentiviral construct (GV492 vector) carrying the full-length mouse HAS2 coding sequence (GenBank: NM_008216.3) was used. Lentiviral particles (titer: 2.00x10^9 TU/ml) were transduced into cells at a multiplicity of infection (MOI) of 50. After 16 h, the medium was replaced with fresh culture medium. Stably transduced cells were selected with 2 μg/ml puromycin starting 72 h post-transduction. Following initial selection, the puromycin concentration was reduced to a maintenance level of 1 μg/ml for continued culture and expansion of the transduced population. For HAS2 knockdown, a short hairpin RNA (shRNA) targeting the sequence 5'-CCTGCCAAGATGTTTGCAATT-3' was cloned into a GV493 lentiviral vector. A non-targeting scramble shRNA (5'-TTCTCCGAACGTGTCACGT-3') served as the negative control. Plasmid (2.5 μg) was transfected into NIH/3T3 cells using Lipofectamine® 3000 (Invitrogen; Thermo Fisher Scientific, Inc.) according to the manufacturer's protocol. Cells were processed for subsequent experiments 24 h post-transfection.

High-throughput virtual screening. High throughput virtual screening was used to screen natural products that can target HAS2 protein. Protein Preparation: The three-dimensional structure of human HAS2 (AlphaFold ID: AF-Q92819-F1) was downloaded from the AlphaFold database (26) and processed using the Protein Preparation Wizard module of Schrödinger Maestro v11.4. The protein was hydrogenated and energy-optimized. Compound Preparation: The 2D structures of compounds from a Natural Product Library (3,995 compounds, MedChemExpress) were hydrogenated and energetically optimized using the LigPrep module of Schrödinger Maestro v11.4 to generate 3D structures for virtual screening. Virtual screening was conducted with the Virtual Screening Workflow module for molecular docking. The prepared compounds were imported for molecular docking using the Glide module, which involved geometric and energetic matching of receptor and ligand. The compounds were screened against HAS2 using standard precision mode. The binding affinities and structures of the top 200 compounds from the natural product library were reviewed based on molecular docking scores for output.

Selection of optimal compounds based on ADME parameters. The top 200 compounds, based on docking scores, were converted to SMILES format and analyzed for ADME parameters using the SwissADME website (http://www.swissadme.ch/). Optimal compounds were selected based on criteria such as lipophilicity (XLOGP3 between -0.7 and +5.0), molecular weight (150-500 g/mol), polarity (TPSA between 20 and 130 $Å^2$), solubility (log S ≤-6), saturation (at least 0.25 fraction of sp^3 hybridized carbons), and flexibility (maximum of 9 rotatable bonds).

Molecular dynamics simulation (MDS) analysis. To elucidate the molecular binding mechanism between OG and HAS2, including key interaction residues, dynamic stability and binding free energy, molecular docking and MDS were conducted using GROMACS v2023.1 (www.gromacs.org). The structures of OG (PubChem CID: 12315192) and HAS2 (PDB ID: Q92819) were retrieved from PubChem (https://pubchem.ncbi.nlm.nih.gov/) and AlphaFold (26), respectively. The systems were solvated in a water box with a 1.0 nm cutoff, using the MMFF and Charmm36 force fields for the protein and TIP3P for water. Electrostatic interactions were calculated with PME, and covalent bonds were constrained using the LINCS algorithm (27). Counter ions (Na^+/Cl^-) were added to neutralize the systems, and energy minimization was carried out using the steepest descent method. After equilibration under NVT conditions, a 100 ps position restraint MDS was performed before production runs in the NPT ensemble with a 2 fsec timestep. Temperature and pressure coupling were achieved using V-rescale and the Parrinello-Rahman barostat. The trajectories were analyzed using VMD v1.9.3 (28), PyMOL v3.1.0 (29) and Origin v2024 (30). Hydrogen bonds were analyzed with the VMD Hydrogen Bonds plugin (28), with stable hydrogen bonds defined as having ≥50% occupancy. The ligand-protein binding free energy was estimated using the MM/PBSA method in GROMACS (31).

Surface plasmon resonance (SPR). To validate the binding affinity and kinetic parameters of OG (MedChemExpress; Purity: 99.57%) to immobilized HAS2, as predicted by computational simulations, SPR analysis was performed using a Biacore T200 system (Cytiva). The CM5 sensor chip (Fc2 channel) was activated with a 400 mM EDC/100 mM NHS mixture (10 μl/min, 800 sec), followed by covalent immobilization of recombinant human HAS2 (100 μg/ml in 10 mM NaAc, pH 4.0) to achieve 10,993 response units. The chip was deactivated by injecting 1 M ethanolamine hydrochloride into both sample channels at 10 μl/min for 800 sec. The running buffer was prepared by mixing PBS-P with 5% DMSO. OG was prepared in seven concentrations (1,250, 625, 312.5, 156.3, 78.2, 39.1, 19.6 and 0 μM) and introduced into the Fc1-Fc2 channels at 30 μl/min for 60 sec to allow binding, followed by a 90-sec dissociation phase.

Cellular thermal shift assay (CETSA). CETSA was performed on cell lysates following the established protocol (32,33). CETSA was employed to confirm the direct binding of OG to HAS2 via ligand-induced thermal stabilization. NIH/3T3 cells were pretreated with 5 ng/ml TGF-β1 for 24 h to upregulate endogenous HAS2 expression, followed by cell collection,

washing with cold PBS, and lysis (with a proteinase inhibitor) through three freeze-thaw cycles. Lysates were centrifuged at 20,000 x g for 20 min at 4˚C to isolate soluble fractions, which were then adjusted to 4 μg/μl (as determined by BCA assay). The lysates were divided into two groups: 100 μM OG treatment or DMSO control (1 h at room temperature). Aliquots were heated at 3˚C intervals (37-70˚C) for 3 min, cooled for 3 min at room temperature, and re-centrifuged (4˚C; 20,000 x g; 20 min). The supernatants were denatured with 5X loading buffer (100˚C for 10 min) and analyzed by western blotting to assess protein stability.

CCK-8 assay. The effect of OG on NIH/3T3 and HFL-1 cell proliferation was evaluated using the CCK-8 assay. Cells were plated at 3,000 cells per well in a 96-well plate, treated with eight drug concentration gradients (0-100 μM), and incubated for 48 h. Afterward, 10 μl of CCK-8 solution (Biosharp Life Sciences) was added to each well, followed by an incubation period of 1-4 h. Absorbance at 450 nm was recorded using a microplate reader.

Animal experimental protocol. Part 1: Time-course analysis of HAS2 and HA dynamics. To delineate the temporal dynamics of HAS2 expression and HA accumulation during fibrotic progression, a cohort of 35 SPF male C57BL/6J mice (6-8 weeks old) was used. Mice were randomly assigned to seven groups (n=5 per group): a saline control group (Day 0) and BLM-treated groups sacrificed at 3, 5, 7, 10, 14, and 21 days post-instillation. Pulmonary fibrosis was induced via a single intratracheal administration of BLM (2 mg/kg) under isoflurane anesthesia (3-4% for induction, 1-1.5% for maintenance); control mice received an equal volume of saline. At each designated endpoint, mice were anesthetized with intraperitoneal injection of pentobarbital sodium (50 mg/kg). After anesthesia induction, sacrifice was performed by exsanguination. Death was confirmed by the absence of spontaneous breathing, heartbeat, and corneal reflex, along with pupillary dilation. Bronchoalveolar lavage fluid (BALF) and lung tissues were then collected for subsequent analysis.

Part 2: Therapeutic efficacy assessment of OG. SPF male C57BL/6J mice (6-8 weeks old) were randomly assigned to six groups (n=8/group) using a computer-generated sequence: i) naïve control (saline vehicle), ii) BLM-induced fibrosis model (untreated), iii) OG-Low (25 mg/kg/day OG), iv) OG-Medium (50 mg/kg/day OG), v) OG-High (100 mg/kg/day OG) and vi) positive control (pirfenidone 100 mg/kg/day). The mice were housed in the SPF-grade animal facility at Shenzhen Glorybay Biotech Co., Ltd., under controlled conditions maintained at a temperature of 22±2˚C, a 12-h light/dark cycle and a humidity of 50±10%. Pulmonary fibrosis was induced in groups 2-6 via intratracheal administration of BLM under isoflurane anesthesia, while control mice received an equivalent volume of saline. Therapeutic interventions were administered daily via oral gavage (0.1 ml/10 g body weight) starting 24 h post-induction, and continued for 14 days, with Groups 1 and 2 receiving volume-matched saline. After two weeks of treatment, anesthesia was induced by an intraperitoneal injection of sodium pentobarbital (50 mg/kg), followed by sacrifice via exsanguination. Serum and lung tissues were then collected for further analysis.

Histological analysis. The left lungs of the mice were preserved in 10% formalin at room temperature for 24 h. The tissues were then dehydrated through a graded ethanol series (70, 80, 95 and 100%), cleared in xylene, and embedded in paraffin. Thin slices of ~4-5 μm were prepared for subsequent staining procedures. Lung injury and inflammation were assessed using hematoxylin and eosin (H&E) staining (performed at room temperature; hematoxylin for 5-8 min, eosin for 1-3 min) to visualize cellular morphology and inflammation. Masson's trichrome staining was performed at room temperature using a commercial kit (Solarbio, Beijing, China) according to the manufacturer's instructions to evaluate collagen deposition in lung tissue samples.

Quantification of OG exposure in serum and lung tissues. To evaluate the systemic and pulmonary exposure of OG following oral administration, OG concentrations in serum and lung tissue homogenates were measured in BLM-induced fibrotic mice treated with OG at three dose levels (25, 50 and 100 mg/kg/day). After 14 days of treatment, blood samples were collected and centrifuged at 2,000 x g for 15 min at 4˚C to obtain serum. The right lung lobes were excised, weighed and homogenized in ice-cold saline using a tissue homogenizer with zirconia beads until a uniform suspension was achieved. OG concentrations in serum and lung homogenates were quantified using a validated ultra-high performance liquid chromatography-tandem mass spectrometry (UHPLC-MS/MS) method. Briefly, the samples were pretreated by protein precipitation with acetonitrile, followed by nitrogen evaporation and reconstitution in 20% methanol. Chromatographic separation was performed on a Waters ACQUITY UPLC HSS T3 column (2.1x100 mm x1.8 μm; Waters China, Ltd.) with gradient elution using acetonitrile and 0.1% formic acid in water. Mass detection was conducted in negative electrospray ionization mode with multiple reaction monitoring (MRM) of the transitions m/z 285.1-123.2 for OG and m/z 271.2-107.8 for the internal standard (arbutin). The method demonstrated good linearity (0.0408-4.08 μg/ml), specificity, and recovery (85-120%) in both matrices.

Statistical analysis. All data are presented as mean ± standard deviation (SD). All reported replicates are independent biological replicates. Statistical analysis was performed using GraphPad Prism (Dotmatics) to identify significant differences. The normality of data distribution was assessed with the Shapiro-Wilk test. For comparisons between two groups, a two-tailed Student's t-test was applied to normally distributed data; otherwise, an appropriate nonparametric test was used. For comparisons among multiple groups, one-way analysis of variance (ANOVA) followed by Tukey's post hoc test was used when the data met normality and homogeneity of variance assumptions; otherwise, the nonparametric Kruskal-Wallis test followed by Dunn's post hoc test was applied. $P<0.05$ was considered to indicate a statistically significant difference.

Results

Cross-species transcriptomics and single-cell resolution analysis reveal fibroblast-specific elevation of HAS2 expression in pulmonary fibrosis. To systematically identify conserved

molecular signatures of IPF pathogenesis, comparative transcriptomic analyses were performed across human clinical samples, animal models and *in vitro* systems. Bioinformatic analysis of the GSE110147 dataset from the GEO database revealed significant dysregulation of 3,499 genes in patients with IPF compared with healthy controls, with 2,170 genes upregulated and 1,329 downregulated (Fig. 1A). A parallel investigation of a BLM-induced pulmonary fibrosis murine model showed similar transcriptional alterations, with 1,058 genes markedly upregulated and 737 downregulated in fibrotic lung tissues relative to healthy controls (Fig. 1B). In complementary cellular experiments, TGF-β1-stimulated myofibroblast differentiation in NIH/3T3 cells resulted in substantial transcriptomic remodeling, with 1,077 genes upregulated and 1,483 downregulated compared with untreated fibroblasts (Fig. 1C). Cross-species comparative analysis identified 17 evolutionarily conserved genes that were consistently upregulated across all three experimental systems (human IPF samples, murine fibrosis models, and TGF-β1-activated myofibroblasts). This core signature of 17 intersecting genes (Fig. 1D) represents potential conserved therapeutic targets for pulmonary fibrosis intervention.

To explore cellular heterogeneity in fibrotic pathogenesis, single-cell transcriptomic profiling was performed on pulmonary tissues from BLM-challenged mice and saline-treated controls. After quality filtering, 76,995 cells were retained and clustered into 32 distinct cell populations (Fig. 1E). The per-sample UMAP embeddings, shown in Fig. S1, demonstrated consistent cell distribution patterns across individual mice within each group. The marker genes defining each of these 32 clusters are listed in Table SII. Cell type annotation was validated through heatmap visualization of canonical marker gene expression for each major cell type (Fig. S2). These clusters were subsequently annotated into 10 major cell types (Fig. 1F), including B cells (15,558 cells), endothelial cells (7,238 cells), epithelial cells (4,383 cells), fibroblasts (2,430 cells), mast cells (368 cells), mononuclear phagocytes (24,214 cells), mural cells (645 cells), neutrophils (5,319 cells), plasmacytoid dendritic cells (4,551 cells) and T cells (12,289 cells). Comparative UMAP visualization revealed conserved clustering patterns for all 10 annotated cell types across control and fibrotic lungs (Fig. 1G). Cell type-specific differential expression analysis identified significant HAS2 upregulation exclusively in the fibroblast populations of BLM-treated mice (Fig. 1H), while expression remained stable across other lineages. This cell type-specific dysregulation corroborated prior bulk transcriptome findings and localized HAS2 hyperactivity to pathogenic fibroblast subsets.

HAS2 and its product HA elevation confirmed in murine and cellular fibrosis models. Bulk transcriptomic and single-cell RNA sequencing analyses clearly indicated that HAS2 is highly expressed in both murine models of pulmonary fibrosis and myofibroblasts. To define the dynamic profile of HAS2 and its product HA during fibrosis development, the present study performed a longitudinal analysis in BLM-challenged mice. Lung tissues and BALF were collected across a time course encompassing the inflammatory and fibrotic phases (Fig. 2A). Western blot analysis revealed that the expression of the fibrotic marker COL1A1 was markedly increased from day 7 onward, peaking at days 14 and 21. HAS2 protein levels exhibited a parallel escalating trend, demonstrating a strong temporal correlation with collagen deposition (Fig. 2B). Notably, HA levels in BALF increased sharply, reaching a peak at day 5 and remained highly elevated throughout the subsequent observation period until day 21 (Fig. 2C), identifying HA as an early-sustained pathogenic component preceding full fibrotic consolidation. To further validate the cellular source of HAS2 upregulation and its association with fibrotic activation, the present study isolated primary lung fibroblasts from control and BLM-treated mice (Fig. 2D). Western blot analysis of these primary cells demonstrated a significant concomitant increase in the protein levels of both COL1A1 and HAS2 in fibroblasts derived from fibrotic lungs compared with those from control lungs (Fig. 2E). Similar results were observed in the TGF-β1-induced myofibroblast model (Fig. 2F). Following stimulation with TGF-β1, the expression of fibrotic markers COL1A1 and ACTA2 in NIH/3T3 fibroblasts was markedly upregulated, indicating their differentiation into myofibroblasts (Fig. 2G). Concomitantly, both HAS2 protein and mRNA levels were markedly increased (Fig. 2G and H). Furthermore, HA levels were markedly increased in the culture medium of myofibroblasts, further supporting the association of HAS2 activity with enhanced HA production (Fig. 2I).

HAS2 in fibroblasts mediates macrophage M2 polarization. To investigate the role of HAS2 in macrophage M2 polarization, shRNA was used to knock down the HAS2 gene in fibroblasts (Fig. 3A). TGF-β1 stimulation markedly increased HA production in fibroblasts. However, when HAS2 was knocked down, the TGF-β1-induced HA production was notably inhibited (Fig. 3B). Subsequently, TGF-β1-stimulated HAS2 knockdown fibroblasts were used to condition the medium for macrophage cultures, followed by flow cytometric analysis of the macrophages (Fig. 3C). The conditioned medium from TGF-β1-stimulated fibroblasts markedly induced M2 polarization in macrophages; however, this effect was markedly reduced when HAS2 was knocked down (Fig. 3D). These results suggested that HAS2 is critical for HA synthesis in response to TGF-β1 stimulation and that downregulating HAS2 impairs the ability of myofibroblasts to induce macrophage M2 polarization.

HA from myofibroblasts induces macrophage M2 polarization via CD44/STAT6 axis. Given their critical role in the fibrotic response, the influence of HA on macrophage polarization was investigated. Agarose gel electrophoresis revealed that the molecular weight of sonicated HA fell within the 10-200 kDa range, confirming it as low-molecular-weight HA (Fig. S3). This sonicated HA was then applied to RAW264.7 mouse monocyte-macrophage cells, and flow cytometry was used to assess macrophage polarization. The results indicated that HA treatment promoted the polarization of RAW264.7 cells towards the M2 macrophage phenotype, as evidenced by increased CD206 expression (Fig. 4A). HA also induced TGF-β1 production in macrophages, further supporting its role in M2 polarization (Fig. 4B). Following HA stimulation, phosphorylation levels of STAT6 progressively increased, suggesting that HA-induced macrophage M2 polarization occurs through the activation of the STAT6 signaling pathway

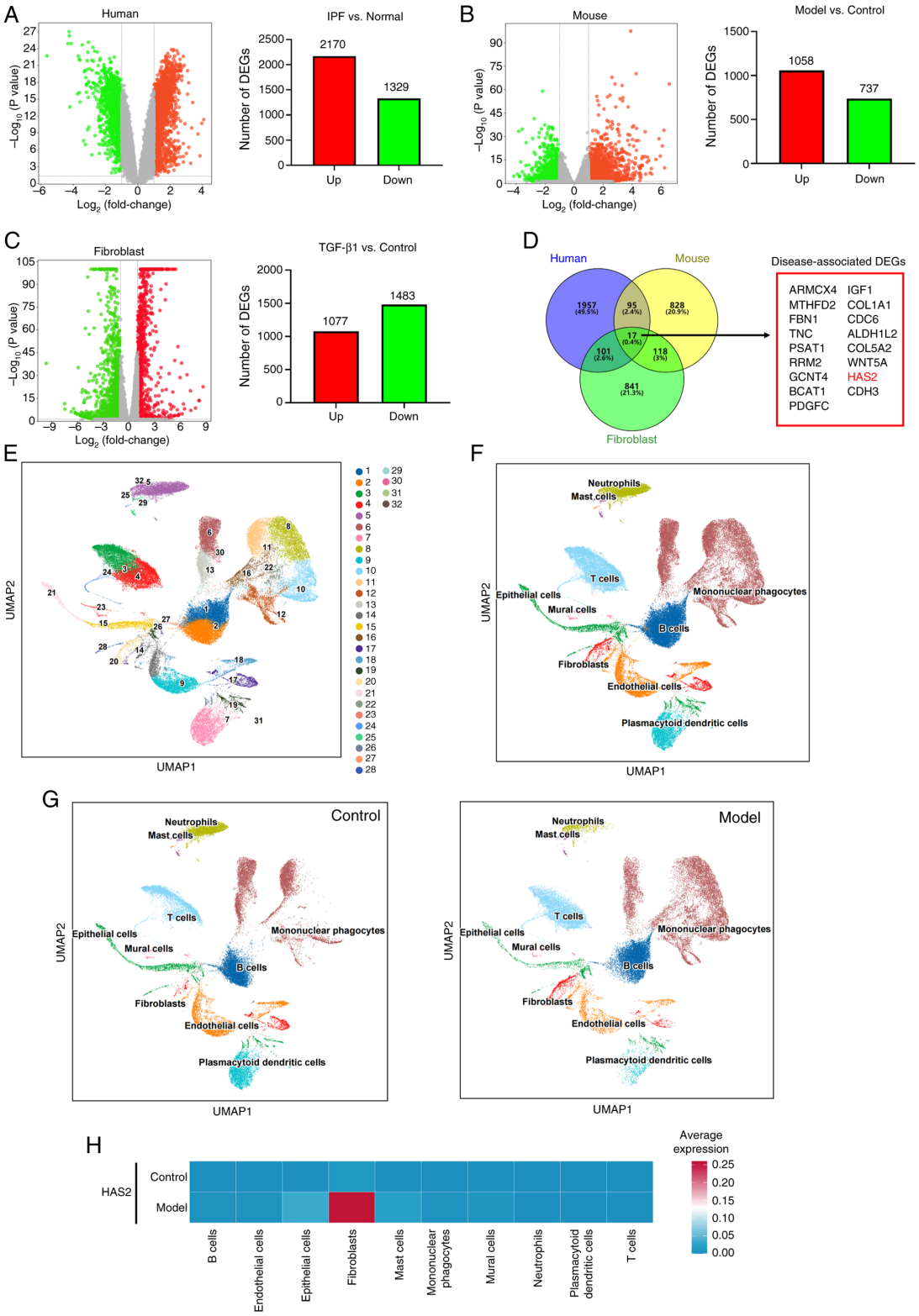

Figure 1. Cross-species transcriptomics and single-cell resolution analysis reveal fibroblast-specific elevation of HAS2 expression in pulmonary fibrosis. (A) Analysis of gene expression profiles from the GSE110147 dataset in the GEO database identified DEGs in patients with IPF (n=22) compared with healthy controls (n=11), with upregulated genes (red) and downregulated genes (green) indicated. (B) Transcriptome sequencing was conducted in a BLM-induced pulmonary fibrosis mouse model to evaluate DEGs by comparing fibrotic mice with normal controls (n=3 for each group), with upregulated genes (red) and downregulated genes (green) indicated. (C) NIH/3T3 cells were stimulated with TGF-β1 to induce myofibroblast transition and transcriptome sequencing was performed to assess DEGs, comparing myofibroblasts to fibroblasts (n=3 for each group). (D) A comprehensive analysis combining data from human, mouse, and cell models to identify key upregulated genes markedly associated with IPF. (E) UMAP plot of 76,995 quality-filtered cells clustered into 32 distinct populations. (F) UMAP visualization annotating clusters into 10 major cell types, with relative cell quantities displayed. Populations include B cells, endothelial cells, epithelial cells, fibroblasts, mast cells, mononuclear phagocytes, mural cells, neutrophils, plasmacytoid dendritic cells, and T cells. (G) Comparative UMAP plots demonstrating conserved spatial distribution of annotated cell types across saline-treated controls and BLM-induced fibrotic lungs (n=3 for each group). (H) Heatmap of cell type-specific HAS2 expression, highlighting significant upregulation exclusively in fibroblast populations of fibrotic lungs. HAS2, hyaluronic acid synthase 2; GEO, Gene Expression Omnibus; DEGs, differentially expressed genes; IPF, idiopathic pulmonary fibrosis; BLM, bleomycin; UMAP, Uniform Manifold Approximation and Projection.

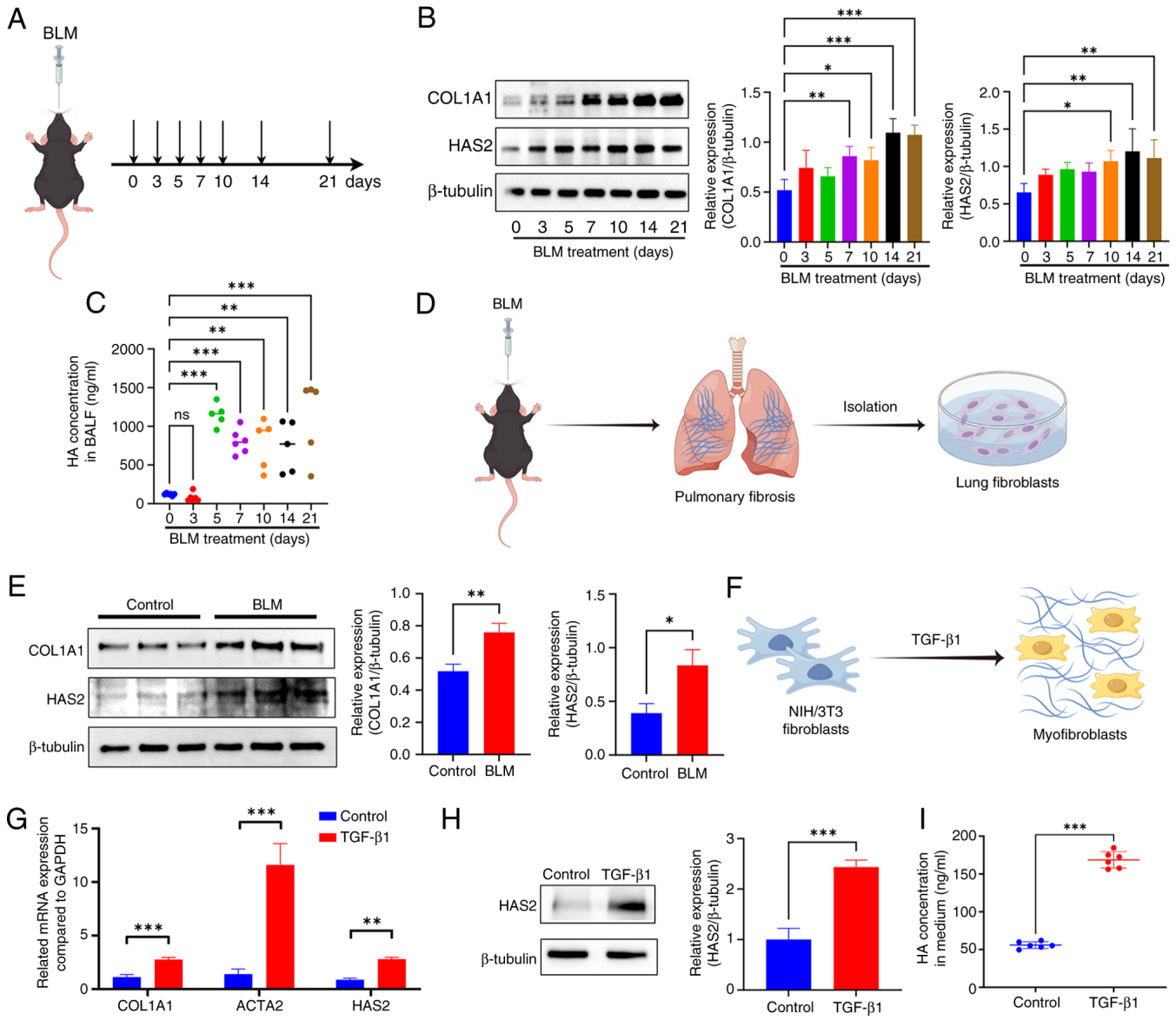

Figure 2. Elevated HAS2 expression and HA accumulation in murine and cellular fibrosis models. (A) Schematic of the experimental design for the time-course study. C57BL/6J mice received a single intratracheal dose of BLM or saline and were sacrificed at the indicated time points (days 0, 3, 5, 7, 10, 14 and 21) for sample collection (n=5 for per group). (B) Representative western blot images (left panel) and densitometric quantification (right panel) showing the protein expression levels of COL1A1 and HAS2 in lung tissues across the time course. β-tubulin served as the loading control (n=4 for per group). (C) ELISA quantification of HA levels in BALF at different days post-BLM injury (n=5 for per group). (D) Schematic diagram illustrating the workflow for the isolation and culture of primary mouse lung fibroblasts from BLM-treated fibrotic mice. (E) Western blotting analysis of HAS2 and COL1A1 protein expression in primary lung fibroblasts isolated from control (saline) and BLM-induced fibrotic mice. Representative blot images (left panel) and densitometric quantification of protein levels normalized to β-tubulin are shown (n=3 for each group). (F) Schematic diagram depicting TGF-β1-induced transition of NIH/3T3 fibroblasts into myofibroblasts. (G) COL1A1, ACTA2, and HAS2 mRNA expression in NIH/3T3 cells was detected using PCR after 5 ng/ml TGF-β1 administration for 12 h (n=3-4 for each group). (H) HAS2 protein expression in NIH/3T3 was detected using western blotting after 5 ng/ml TGF-β1 administration for 24 h (n=3 for each group). (I) ELISA was used to quantify HA concentrations in the culture media of myofibroblasts (n=6 for each group). *P<0.05, **P<0.01, ***P<0.001. HAS2, hyaluronic acid synthase 2; HA, hyaluronic acid; BLM, bleomycin; BALF, bronchoalveolar lavage fluid; COL1A1, Collagen type I α 1 chain; ACTA2, actin alpha 2, smooth muscle.

(Fig. 4C). CD44, the receptor through which HA binds to cells, was implicated in this process. Inhibition of CD44 markedly reduced HA-induced CD206 expression in macrophages (Fig. 4D), as well as suppressed TGF-β1 expression and STAT6 phosphorylation levels (Fig. 4E and F). To confirm the necessity of STAT6 activation, pharmacological inhibition of STAT6 (AS1517499) effectively blocked HA-induced STAT6 phosphorylation (Fig. 4G). To validate this signaling axis in a more physiologically relevant context, a fibroblast-macrophage co-culture system was employed (Fig. 4H). Conditioned medium from TGF-β1-stimulated NIH/3T3 fibroblasts strongly induced M2 polarization in RAW264.7 macrophages. This effect was substantially diminished when macrophages were co-treated with either a CD44 inhibitor or a STAT6 inhibitor (Fig. 4I). These results demonstrate that HA induces macrophage M2 polarization by binding to CD44 on macrophages and activating the STAT6 pathway.

High-throughput virtual screening and target validation experiments identified OG as a natural HAS2 inhibitor.

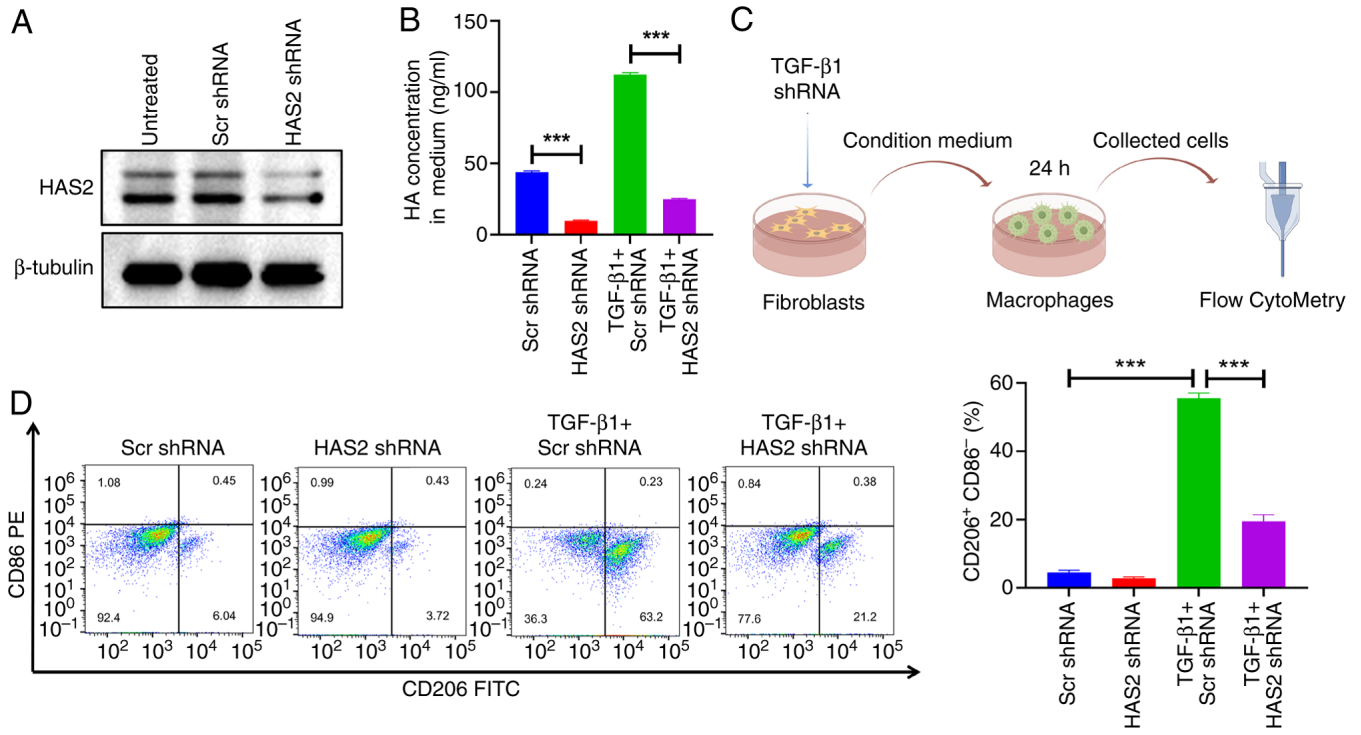

Figure 3. HAS2 in fibroblasts mediates macrophage M2 polarization. (A) Western blotting of HAS2 expression in NIH/3T3 fibroblasts transduced with lentiviral vectors carrying shRNA targeting HAS2. Scramble shRNA and untreated cells were used as controls. (B) ELISA quantification of HA levels in supernatants collected 24 h after TGF-β1 stimulation of NIH/3T3 fibroblasts transduced with HAS2-targeting or scramble shRNA vectors (n=3 for each group). (C) Schematic workflow: Conditioned medium from TGF-β1-stimulated, HAS2-knockdown NIH/3T3 fibroblasts was used to culture RAW264.7 macrophages for 24 h, followed by flow cytometric analysis of macrophage polarization. (D) Flow cytometry was used to measure the expression levels of CD206 (FITC) and CD86 (PE) (n=3 for each group). ***P<0.001. HAS2, hyaluronic acid synthase 2; shRNA, short hairpin RNA; HA, hyaluronic acid; FITC, fluorescein isothiocyanate; PE, phycoerythrin.

A high-throughput virtual screening of natural compounds was conducted to identify small molecules that can bind to the HAS2 protein (Fig. 5A and B). After the initial screening, the top 200 compounds were selected based on docking scores for further analysis. These compounds were then evaluated using ADME parameters to identify those with favorable drug-like properties. Among the 200 compounds, only OG met all the ADME screening criteria, highlighting its potential as a HAS2-targeting compound with favorable drug-like properties (Fig. 5C). The molecular formula of OG is shown in Fig. 5D and its docking score with HAS2 is-7.325. The physicochemical properties of OG include: XLOGP3 (-0.99), molecular weight (286.28 g/mol), TPSA (119.61 Å^2), log S (-1.02), Fraction Csp3 (0.54), and 3 rotatable bonds. To assess the binding affinity between HAS2 and OG, an SPR experiment was performed (Fig. 5E). The association rate constant (Ka) was 20.66 $M^{-1}sec^{-1}$, and the dissociation rate constant (Kd) was 0.006278 sec^{-1}. The dissociation constant was calculated to be 3.039x10^{-4} M, confirming a direct binding interaction between HAS2 and OG. Further validation using CETSA showed that OG enhanced HAS2 protein stability under rising temperatures compared with the control group, reinforcing the direct interaction between OG and HAS2 (Fig. 5F). The SPR and CETSA experiments confirm that OG binds directly to the HAS2 protein.

A CCK-8 assay was performed to assess the cytotoxic effects of OG on murine NIH/3T3 and human HFL-1 fibroblast cell lines. The results (Fig. 5G) indicated that OG was non-toxic to these cell lines at concentrations ranging from 0 to 100 μM. TGF-β1-stimulated NIH/3T3 and HFL-1 cells were then treated with varying concentrations of OG, and ELISA was performed to measure HA content in the cell culture supernatant. The results showed that OG effectively and concentration-dependently inhibited HA secretion, with half-maximal inhibitory concentrations (IC_{50}) of 28.19 μM and 31.11 μM for NIH/3T3 and HFL-1 cells, respectively (Fig. 5H). Additionally, lentiviral vectors were used to overexpress the HAS2 protein in NIH/3T3 cells (Fig. 5I). HAS2 overexpression markedly increased HA production, whereas OG treatment effectively inhibited this increase (Fig. 5J). These results suggested that OG targets HAS2 to suppress HA production.

MDS indicated the binding stability of OG and HAS2. MDS confirmed stable binding between OG and HAS2 (Fig. 6A), with hydrophobic interactions and hydrogen bonds formed with key residues (Fig. 6B and C). Hydrogen bond occupancy analysis identified ASP313 (137.60%) and ASP121 (110.10%) as primary stable binding sites, with an average of five hydrogen bonds maintained throughout the >40 nsec simulation (Fig. 6D). Hydrogen bond occupancy was calculated as the percentage of simulation frames in which a specific atom pair formed a hydrogen bond. Occupancies >100% indicate that the residue formed multiple, concurrent hydrogen bonds with the ligand within individual frames, reflecting a high-density interaction interface. A complete list of

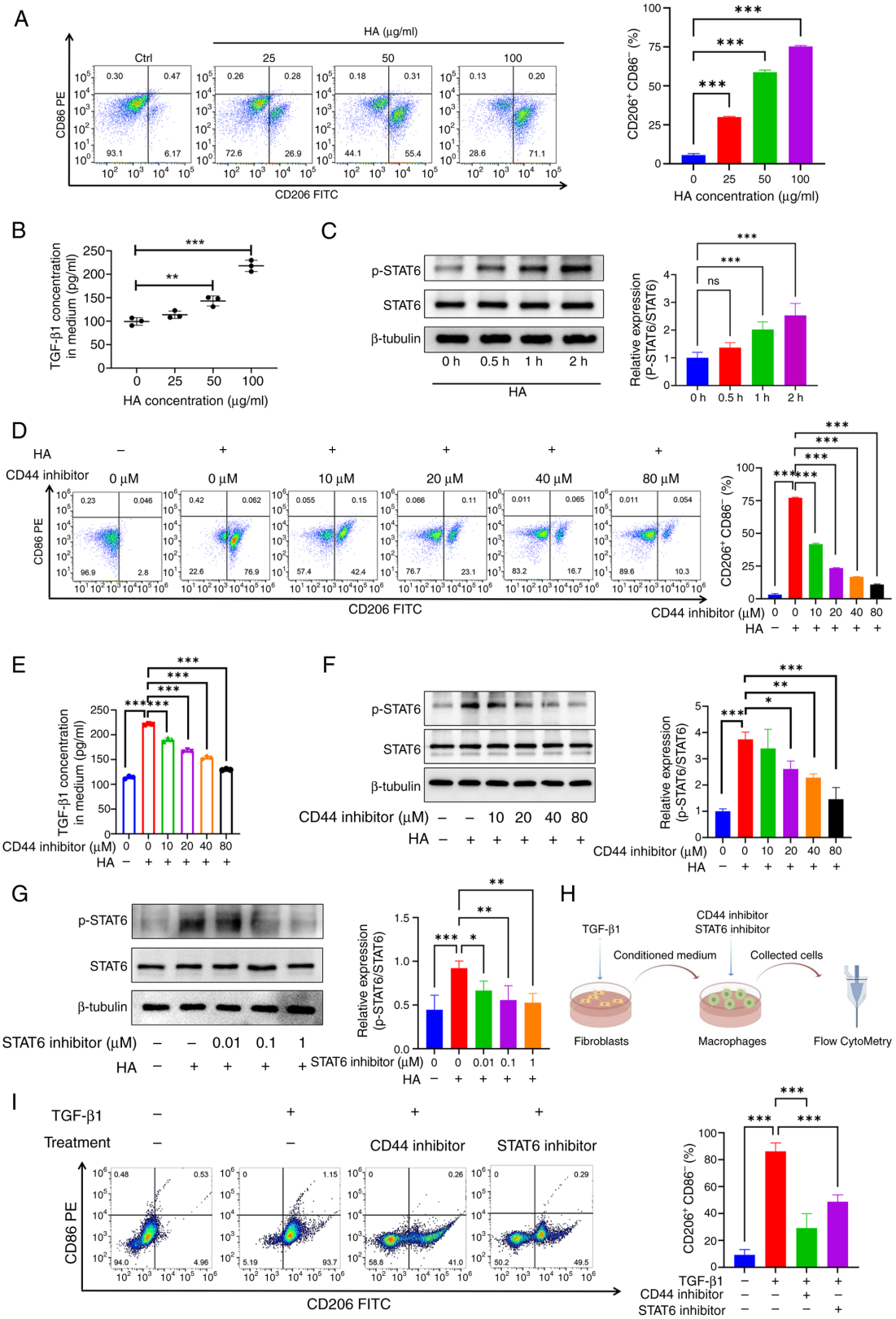

Figure 4. HA from myofibroblasts induces macrophage M2 polarization via the CD44/STAT6 axis. (A) RAW264.7 macrophages were stimulated with HA for 24 h, and flow cytometry was performed to assess the expression of CD206 (FITC) and CD86 (PE) (n=3 for each group). (B) The content of TGF-β1 in macrophages following HA treatment over 48 h was quantified using ELISA (n=3 for each group). (C) Western blotting analysis of p-STAT6 and total STAT6 expression at various time points following 100 μg/ml HA stimulation (n=4 for each group). (D) Flow cytometric analysis of CD86 and CD206 expression in macrophages after 24-h treatment with 100 μg/ml HA and CD44 inhibitor at indicated concentrations (n=3 for each group). (E) TGF-β1 quantification by ELISA in culture supernatants (n=3 for each group). (F) Western blotting analysis of p-STAT6 and total STAT6 in macrophages following 2-h treatment with HA and CD44 inhibitor at varying concentrations (n=3 for each group). (G) Western blotting analysis of p-STAT6 and total STAT6 in macrophages following 2-h treatment with HA and STAT6 inhibitor (AS1517499) at varying concentrations (n=4 for each group). (H) Schematic workflow: Conditioned medium from TGF-β1-stimulated NIH/3T3 fibroblasts was used to culture RAW264.7 macrophages for 24 h. Where indicated, RAW264.7 cells were co-treated with a CD44 inhibitor or a STAT6 inhibitor. Macrophage polarization was subsequently analyzed by flow cytometry. (I) Flow cytometry was used to measure the expression levels of CD206 (FITC) and CD86 (PE) (n=3 for each group). *P<0.05, **P<0.01, ***P<0.001. HA, hyaluronic acid; FITC, fluorescein isothiocyanate; PE, phycoerythrin; p-, phosphorylated.

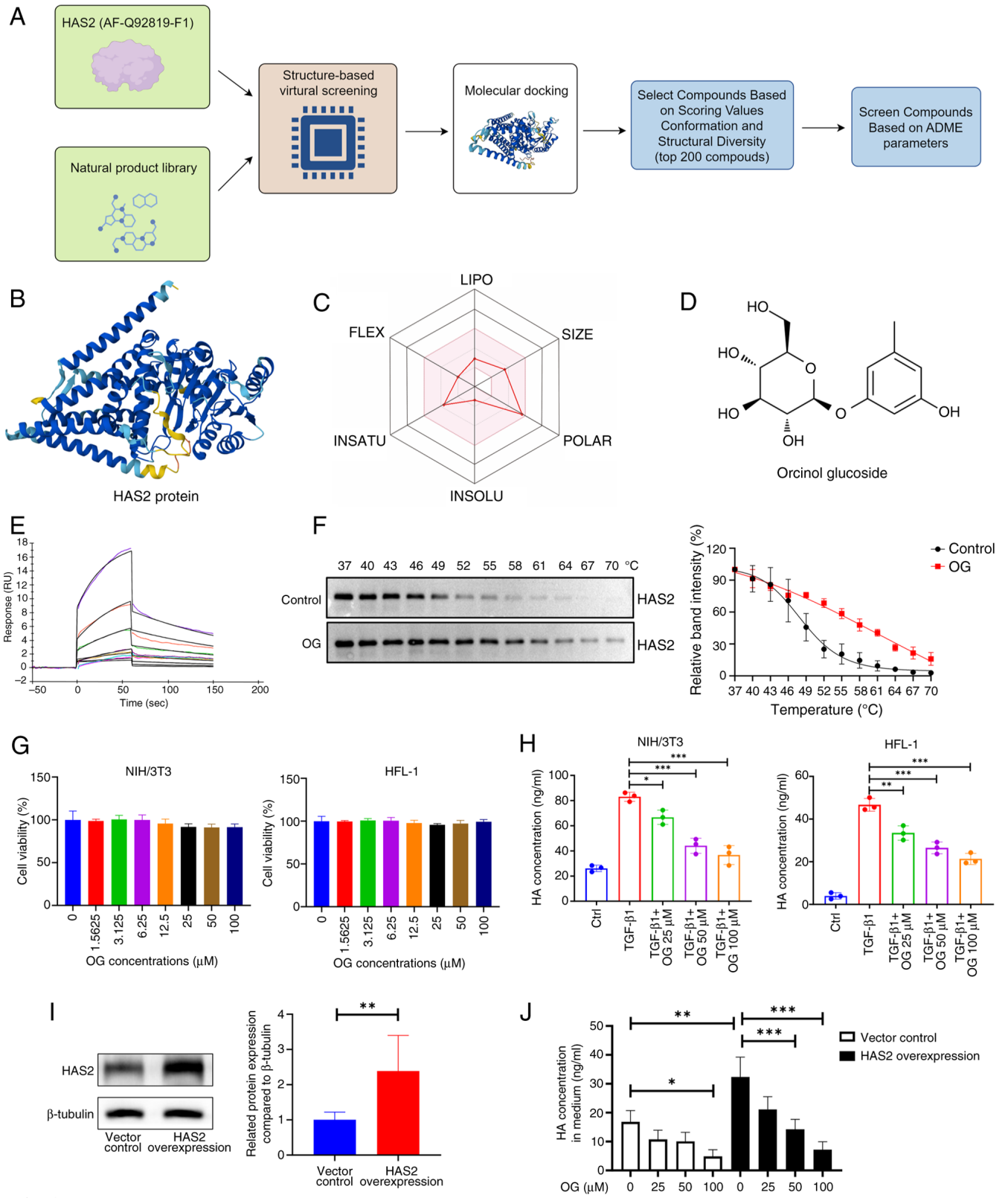

Figure 5. High-throughput virtual screening and target validation experiments identifies OG as a natural HAS2 inhibitor. (A) Flowchart outlining the high-throughput virtual screening process. (B) The three-dimensional structure of human HAS2 was obtained from the AlphaFold database (AlphaFold ID: AF-Q92819-F1). (C) The radar map shows that OG met the ADME criteria. (D) The molecular formula of OG is illustrated. (E) SPR experiment was conducted to determine the binding affinity of OG to HAS2, providing quantitative data on binding kinetics. (F) CETSA assay was performed to confirm the direct interaction between OG and HAS2, showing enhanced protein stability upon OG treatment (n=3 for each group). (G) The cytotoxicity of OG was assessed using CCK-8 assays on NIH/3T3 and HFL-1 cell lines following a 48-h treatment at various concentrations (n=3-6 for each time point). (H) ELISA assays were performed to quantify HA levels in the supernatant of TGF-β1-stimulated NIH/3T3 and HFL-1 cells treated with OG for 48 h (n=3 for each group). (I) Lentiviral vectors were used to overexpress HAS2 in NIH/3T3 fibroblasts, with western blotting conducted to confirm HAS2 expression levels (n=6 for each group). (J) OG was administered to both HAS2-overexpressing NIH/3T3 cells and control cells without overexpression. After a 48-h treatment with OG, ELISA was used to measure the HA content in the culture medium (n=3 for each group). *P<0.05, **P<0.01, ***P<0.001. OG, glucoside; HAS2, hyaluronic acid synthase 2; ADME, absorption, distribution, metabolism and excretion; SPR, surface plasmon resonance; CETSA, cellular thermal shift assay.

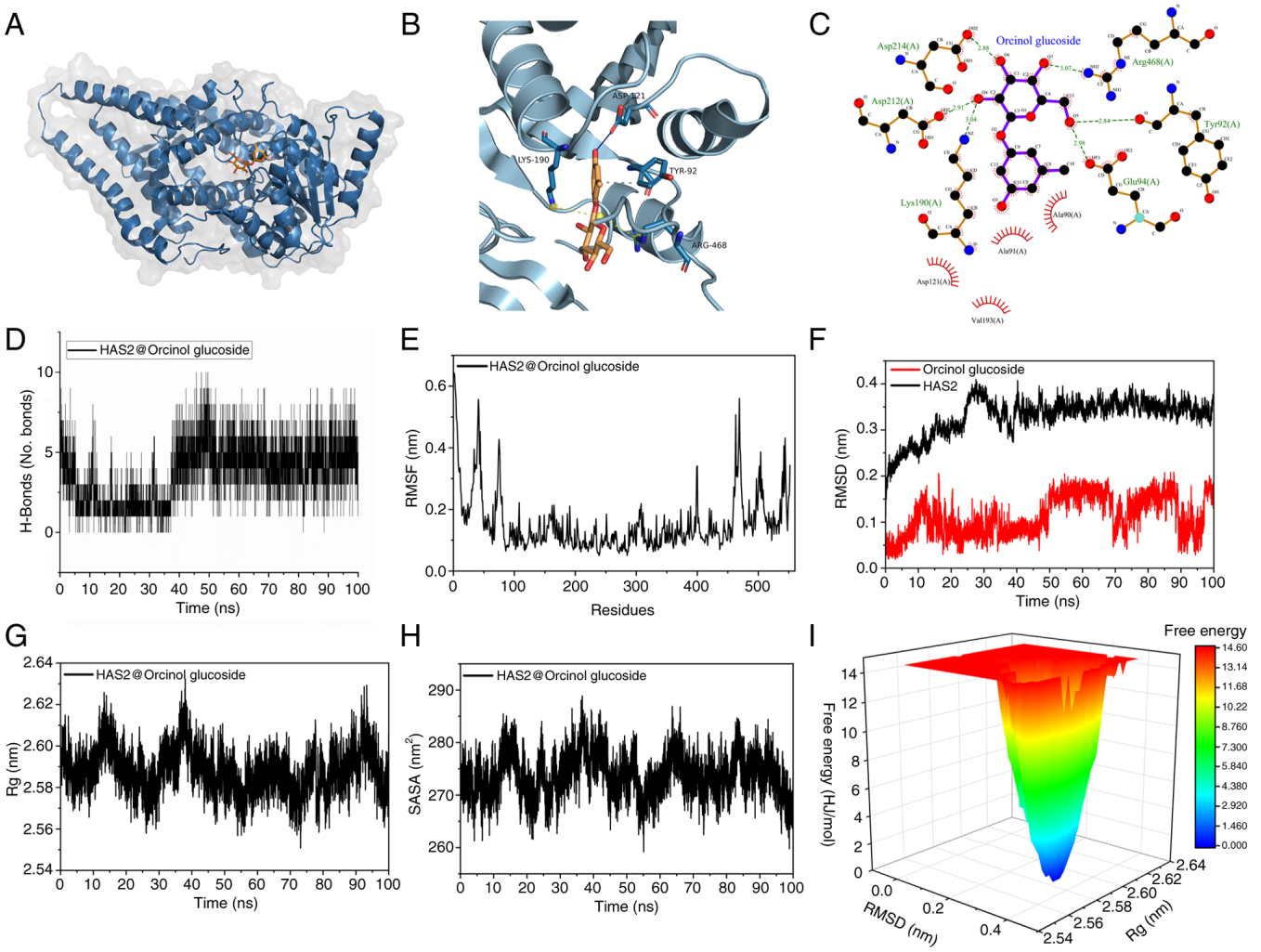

Figure 6. MDS indicates the binding stability of OG and HAS2. (A) The lowest energy binding position of OG and HAS2. (B and C) Hydrogen bond interactions at the lowest energy binding position between OG and HAS2. (D) Hydrogen bond analysis between OG and HAS2. (E) RMSF analysis of the bound complex of OG and HAS2. (F) RMSD trajectory analysis of the bound complex of OG and HAS2. (G) Rg analysis of the bound complex of OG and HAS2. (H) SASA analysis of the bound complex of OG and HAS2. (I) Frames at the minimal free energy landscape for the bound complex of OG and HAS2. MDS, molecular dynamics simulation; OG, glucoside; HAS2, hyaluronic acid synthase 2; RMSF, root-mean-square fluctuations; SASA, solvent accessible surface area.

hydrogen bonds and a time-resolved occupancy heatmap are provided in Table SIII and Fig. S4. Conformational stability was confirmed by low root-mean-square fluctuations (RMSF) values across 100 nsec, indicating minimal protein flexibility, except for residues near positions 30, 70, 400, 470 and 500 (Fig. 6E). Root-mean-square deviation (RMSD) analysis showed stable binding conformations (0.1-0.4 nm) after the initial 10 nsec, with consistent radius of gyration and solvent-accessible surface area values, confirming no major structural changes (Fig. 6F-H). Free energy landscape analysis identified the lowest energy binding conformation at 24.12 ns (39.954 kJ/mol), further supporting the stable OG-HAS2 interaction (Fig. 6I).

OG exerts an anti-pulmonary fibrosis effect by impairing myofibroblast-mediated macrophage M2 polarization. To further investigate the role of OG in macrophage M2 polarization, fibroblasts were treated with OG during TGF-β1 stimulation. The conditioned medium was collected and used to culture macrophages, followed by ELISA and flow cytometric analysis (Fig. 7A). The results showed that conditioned medium from TGF-β1-stimulated fibroblasts markedly induced macrophage M2 polarization; however, this effect was markedly reduced with OG treatment. Conditioned medium from OG-treated fibroblasts showed markedly reduced capacity to induce TGF-β1 release from macrophages (Fig. 7B). Similarly, the ability of this conditioned medium to stimulate CD206 expression in macrophages was substantially impaired (Fig. 7C). These results demonstrated that OG inhibited the ability of myofibroblasts to induce macrophage M2 polarization.

A BLM-induced mouse model was used to assess the anti-fibrotic effects of OG on the lungs. Histological analysis with H&E and Masson's trichrome staining showed that OG treatment mitigated pulmonary inflammation and fibrosis progression in the mouse model (Fig. 7E). Immunoblotting of lung tissues demonstrated that OG inhibited the expression of fibrotic markers, including COL1A1 and α-SMA (Fig. 7F). Furthermore, OG markedly reduced the levels of HA and TGF-β1 in the mice (Fig. 7G and H). Quantitative

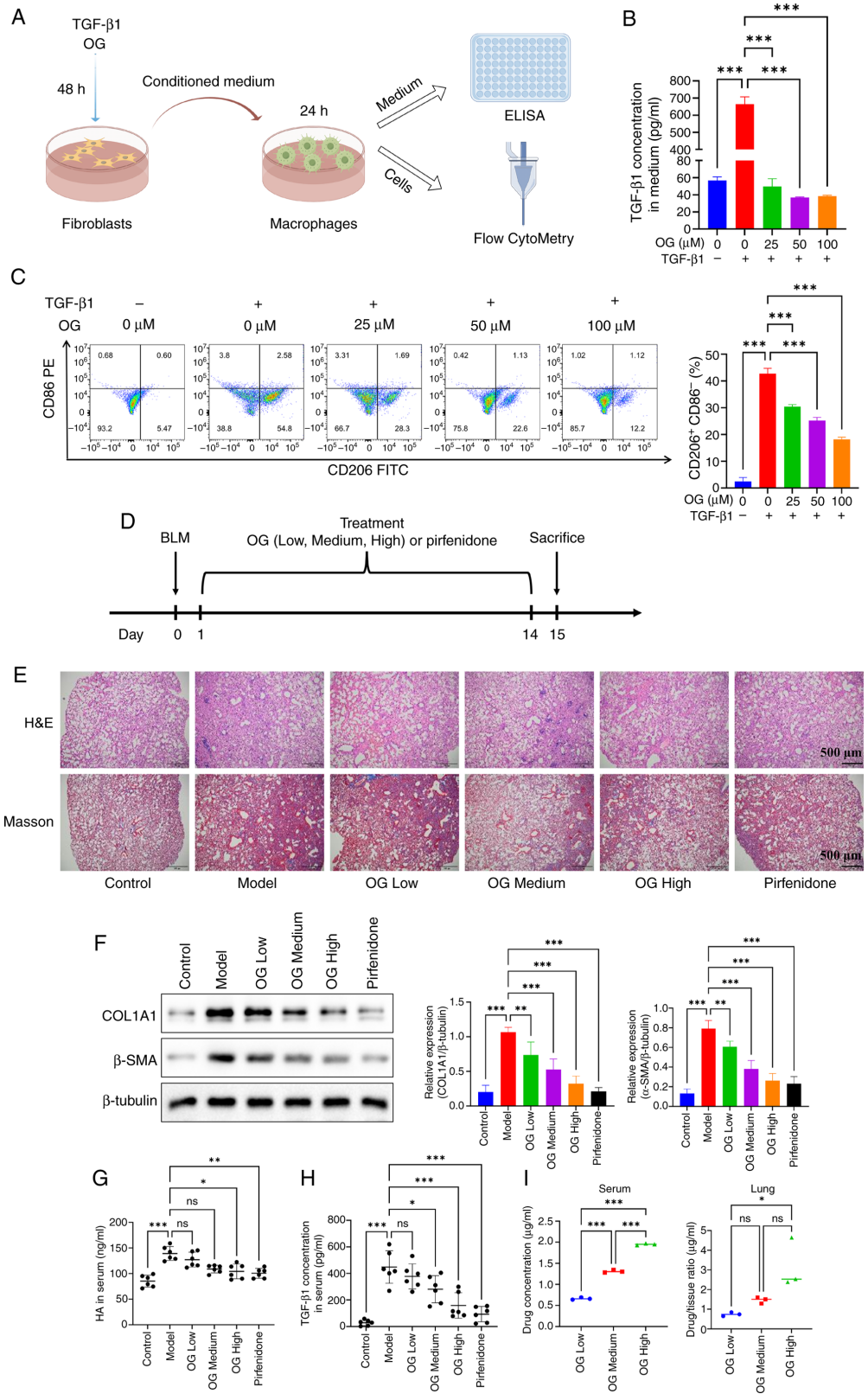

Figure 7. OG exerts an anti-pulmonary fibrosis effect by impairing myofibroblast-mediated macrophage M2 polarization. (A) Schematic workflow: Fibroblast treatment with OG during TGF-β1 stimulation, followed by conditioned medium collection and macrophage culture for downstream assays. (B) TGF-β1 release from macrophages measured by ELISA (n=3 for each group). (C) Flow cytometric analysis of CD206 and CD86 expression in macrophages cultured in conditioned medium. The bar graph quantifies the proportion of $CD206^{+}CD86^{-}$ cells (M2-like macrophage subpopulation; n=3 for each group). (D) Animal experimental protocol. (E) A BLM-induced mouse model was established to assess the anti-fibrotic effects of OG. Histopathological alterations in lung tissues from different groups were assessed using H&E and Masson's trichrome staining. Scale bars: 500 μm; magnification, x40. (F) Western blotting analysis to measure the expression levels of fibrotic markers, COL1A1 and α-SMA, in lung tissues (n=4 for each group). (G) The levels of HA in mouse serum were quantified by ELISA. (H) The levels of TGF-β1 in mouse serum were quantified by ELISA (n=6 for each group). (I) OG concentrations in serum and lung tissues after 14-day oral administration. Left: serum concentrations of OG across treatment groups. Right: lung tissue concentrations of OG, expressed as a percentage of tissue weight (n=3 for each group). *P<0.05, **P<0.01, ***P<0.001. OG, glucoside; BLM, bleomycin; COL1A1, Collagen type I α 1 chain; α-SMA, α-smooth muscle actin; H&E, hematoxylin and eosin.

analysis of OG concentrations in serum and lung tissues revealed dose-proportional increases in both compartments (Fig. 7I). This dose-dependent tissue distribution of OG paralleled its graded therapeutic efficacy, establishing a clear exposure-response relationship across treatment groups.

Discussion

The present study aimed to identify key pathogenic factors in IPF and explore novel therapeutic strategies targeting HA metabolism. The integrated findings highlighted HAS2 as a central driver of IPF pathogenesis, promoting HA accumulation and macrophage M2 polarization through a CD44-dependent STAT6 activation pathway. OG was identified as a natural product that binds to HAS2 and alleviates pulmonary fibrosis by disrupting this pathogenic axis in both *in vitro* and *in vivo* models. These results position HAS2 as a promising therapeutic target and OG as a potential candidate for IPF treatment.

Transcriptional landscape analyses of human IPF samples, murine fibrosis models and TGF-β1-induced myofibroblasts revealed that HAS2 is consistently upregulated, with single-cell RNA sequencing localizing this elevation specifically to fibroblasts. This cell type-specific dysregulation is biologically significant, as fibroblasts are key mediators of ECM deposition in IPF (34). The validation experiments of the present study confirmed that HAS2 upregulation is linked to increased HA production in fibrotic tissues and cells, consistent with clinical observations that HA levels correlate with IPF severity (35). Mechanistically, fibroblast-derived HA induced macrophage M2 polarization through CD44 binding and subsequent STAT6 phosphorylation. This polarization is a critical event in the maintenance of the fibrotic niche, shedding light on a previously undefined crosstalk between stromal cells and immune cells in fibrosis, where HAS2-mediated HA acts as a paracrine signal to amplify pro-fibrotic inflammation (36,37). These findings are further corroborated by complementary *in vitro* data. As shown in Fig. S5, HA stimulation alone effectively induced TGF-β1 release from macrophages, with a potency comparable to that of the classical M2-polarizing cytokines IL-4/IL-13. These results indicated that fibroblast-derived HA itself acted as a potent M2-polarizing stimulus, functionally akin to traditional immune cytokines, and can synergize with immune signals in the pathological microenvironment to collectively drive and sustain a pro-fibrotic macrophage phenotype.

The identified interaction is not unidirectional but forms a self-amplifying positive feedback loop that drives fibrotic progression. Activated fibroblasts, via HAS2-derived HA, polarize macrophages toward a pro-fibrotic M2 phenotype in a CD44/STAT6-dependent manner. In turn, these M2-polarized macrophages release factors such as TGF-β1, further activating fibroblasts, promoting their transition to myofibroblasts, and driving excessive ECM deposition. This 'fibroblast-macrophage' vicious cycle aligns with and extends the understanding of the complex cellular crosstalk in pulmonary fibrosis. For instance, work by Liu *et al* (38) highlights the protective, multi-faceted role of the TWEAK-Fn14 signaling axis, which inhibits fibroblast activation and ECM synthesis while recruiting and modulating macrophage subsets to influence alveolar repair, highlighting the bidirectional and multi-layered nature of stromal-immune interactions. Similarly, in other fibrotic contexts such as silicosis, aberrant macrophage activation (e.g., via the PRDX4-AKT/NF-κB or Lp-PLA2-mitophagy pathways) has been shown to drive the aberrant transformation of epithelial cells and fibroblasts (39,40). Targeting critical nodes within this feedback loop, such as HAS2 in the present study, represents a precise therapeutic strategy to disrupt the self-perpetuating cycle of fibrosis.

Comparisons with existing literature highlight the novelty of the present study. While HA elevation in IPF is well-documented, a prior study has have primarily focused on total HA levels without distinguishing the contributions of specific HAS isoforms (7). The present study identified HAS2 as the functionally dominant isoform in fibrotic lungs, extending earlier reports that HAS2 is the most active synthase in HA production (10). Unlike 4-methylumbelliferone, a widely studied HA inhibitor that depletes UDP-glucuronic acid and downregulates HAS2/3 expression (41), OG binds directly to HAS2, as evidenced by stable interactions with key residues (ASP313 and ASP121), confirmed by MDS and biophysical assays. This direct binding mechanism may offer target selectivity, potentially avoiding broader off-target effects associated with substrate depletion. Computational molecular docking provided preliminary support for this selectivity, predicting that OG exhibits the strongest binding affinity for HAS2 (binding energy: -7.777 kcal/mol), compared with HAS1 (-6.715 kcal/mol) and HAS3 (-6.486 kcal/mol) (Fig. S6). *In silico*, a binding energy below -7.0 kcal/mol is often considered indicative of good binding affinity, suggesting OG preferentially engages HAS2. However, comprehensive biochemical profiling of its isoform selectivity and inhibition kinetics remains a critical direction for future research. Furthermore, while current IPF therapies such as pirfenidone and nintedanib broadly inhibit fibrosis progression without targeting specific pathogenic drivers (12), the approach of the present study directly targeted a defined molecular axis, offering a more precise therapeutic strategy. OG, a natural phenol glycoside derived from *Curculigo orchioides* Gaertn., benefits from the extensive traditional medicinal use and established safety profile of its source in treating rheumatological and respiratory conditions, enhancing OG's translational viability compared with novel synthetic compounds (42-46). The present study also analyzed the correlation between OG's tissue distribution and its *in vivo* efficacy. Quantification confirmed that OG achieved dose-dependent concentrations in systemic circulation and, importantly, was detectable in lung tissue, the primary site of pathology. This graded pulmonary exposure of OG corresponded with the attenuation of fibrotic markers (COL1A1, α-SMA), collagen deposition and key pro-fibrotic mediators (HA and TGF-β1).

The biological relevance of the present study extended beyond pulmonary fibrosis. The HAS2-HA axis has also been implicated in hepatic fibrosis, where HAS2 overexpression activates hepatic stellate cells via CD44 and Notch1 signaling and genetic ablation of HAS2 alleviates liver fibrosis in murine models (47). This cross-organ conservation suggests that HAS2-targeted therapies could have broad applications in fibrotic disorders. Clinically, OG's favorable safety profile in cellular models and its ability to reduce collagen deposition

and inflammatory markers *in vivo* support its potential as a therapeutic agent. Additionally, the correlation between serum HA levels and treatment response in our murine model suggests that HA could serve as a pharmacodynamic biomarker, facilitating clinical monitoring of therapeutic efficacy (35).

The present study had several limitations. First, while the BLM-induced fibrosis model is widely used, it does not fully replicate the chronic, progressive nature of human IPF and lacks the pathological heterogeneity seen in clinical settings (48). Future validation in alternative models, such as TGF-β transgenic mice or precision-cut lung slices from patients with IPF, would enhance clinical relevance. Second, macrophage polarization states in lung tissues of the mouse model were not directly evaluated. Future studies employing detailed immunophenotyping of lung immune cells will provide direct *in vivo* evidence to complement the functional and biochemical data of the present study. Third, the *in vitro* mechanistic studies of the present study relied on the RAW264.7 murine cell line; validating key findings in primary murine bone marrow-derived macrophages and human monocyte-derived macrophages is essential for establishing the translational relevance of the HA-CD44-STAT6 axis. Fourth, the present study did not perform direct *in vitro* enzymatic inhibition assays using recombinant HAS2 protein due to the technical challenge of expressing and purifying functional full-length HAS2, a multi-pass transmembrane enzyme. While SPR binding, CETSA target engagement and cellular assays confirmed that OG suppresses HA synthesis by targeting HAS2, novel strategies to assess HAS2 activity will further validate our mechanistic conclusions. Lastly, the *in vivo* therapeutic regimen of the present study focused on preventive/early intervention (OG administered 24 h post-BLM injury, prior to peak fibrosis) and did not model late-stage fibrotic disease reversal. Future studies with dosing initiated after full fibrosis establishment (such as 7 days post-injury) are crucial to define the translational potential of OG and other HAS2-targeting agents for IPF.

In conclusion, the present study identified HAS2 as a critical regulator of fibroblast-immune crosstalk in IPF. OG suppresses this pathway by targeting HAS2. These findings advance our understanding of IPF pathogenesis and provide a preclinical foundation for targeting HAS2 in fibrotic diseases. Future research should focus on optimizing OG's pharmacokinetic properties, evaluating its efficacy in clinically relevant models, and exploring combination therapies with existing antifibrotic agents to enhance therapeutic outcomes. By targeting the HAS2-HA-macrophage axis, this work opens new avenues for developing precision therapies for IPF and other fibrotic disorders.

Acknowledgements

Some figures (Figs. 2A, D, F, 3C, 4H, 5A and 7A) were created with Figdraw (https://www.figdraw.com). The authors thank Figdraw for providing the authorization to use these figures.

Funding

The present study was supported by the Guangdong Basic and Applied Basic Research Foundation (grant no. 2023A1515011243); Shenzhen Science and Technology Program (grant no. JCYJ20240813153503005); Bao'an Traditional Chinese Medicine Development Foundation (grant no. 2022KJCX-ZJZL-11); Health and Medical Scientific Research Project of Shenzhen Bao'an Medical Association (grant no. BAYXH2024017); Shenzhen Bao'an Traditional Chinese Medicine Hospital Research Program (grant no. BAZYY20220701); 2024 High-quality Development Research Project of Shenzhen Bao'an Public Hospital (grant no. BAGZL2024137); Discipline Construction Program of the University-Hospital Collaborative Project in the Development of High-Level University (grant no. GZYBA2024XKG02); and The Sanming Project of Medicine in Shenzhen (grant no. SZZYSM202206013).

Availability of data and materials

The data generated in the present study may be requested from the corresponding author. The transcriptome sequencing datasets generated in the present study are publicly available in the NCBI Sequence Read Archive (SRA) under the following accession numbers: PRJNA782761 (for TGF-β1-induced myofibroblasts) and PRJNA1301583 (for the BLM-induced pulmonary fibrosis mouse model). The single-cell RNA sequencing dataset is available in the NCBI SRA under accession number PRJNA1392040. The raw UHPLC-MS/MS data for quantitative analysis are available in the MassIVE repository under accession number MSV000100304. The persistent URLs for these datasets are: https://www.ncbi.nlm.nih.gov/bioproject/PRJNA782761; https://www.ncbi.nlm.nih.gov/bioproject/PRJNA1301583; https://www.ncbi.nlm.nih.gov/bioproject/PRJNA1392040; ftp://massive-ftp.ucsd.edu/v11/MSV000100304.

Authors' contributions

CL, XT and XLu conceived and designed the study, performed the experiments, analyzed the data and drafted the manuscript. XLa, JY, ZX and GM performed the experiments, collected data and assisted with data analysis. YX performed the formal analysis and data interpretation. XH supervised the research, acquired funding and critically reviewed and edited the manuscript. HL administered the project, designed the methodology, drafted the manuscript and acquired funding. XLa and HL confirm the authenticity of all the raw data. All authors read and approved the final manuscript.

Ethics approval and consent to participate

The animal experiments were conducted at external SPF-grade facilities due to the lack of such a facility at our institution. All animal experiments were approved by the Ethics Committee of the Animal Subjects Ethics Sub-committee of the Hong Kong Polytechnic University (ethics number: 22-23/356-OTHERS-R-NSFC) and the Ethics Committee of Shenzhen Glorybay Biotech Co., Ltd (approval nos. RW-IACUC-24-0037 and RW-IACUC-25-0065).

Patient consent for publication

Not applicable.

Competing interests

The authors declare that they have no competing interests.

References

1. Strongman H, Kausar I and Maher TM: Incidence, prevalence, and survival of patients with idiopathic pulmonary fibrosis in the UK. Adv Ther 35: 724-736, 2018.
2. Ma HY, Li Q, Wong WR, N'Diaye EN, Caplazi P, Bender H, Huang Z, Arlantico A, Jeet S, Wong A, *et al*: LOXL4, but not LOXL2, is the critical determinant of pathological collagen cross-linking and fibrosis in the lung. Sci Adv 9: eadf0133, 2023.
3. Mei Q, Yang Z, Xiang Z, Zuo H, Zhou Z, Dong X, Zhang L, Song W, Wang Y, Hu Q, *et al*: Pharmacological inhibition of MDM4 alleviates pulmonary fibrosis. Theranostics 13: 2787-2799, 2023.
4. Zhang X, Hu X, Zhang Y, Liu B, Pan H, Liu Z, Yao Z, Zhu Q, Wu C and Shen T: Impaired autophagy-accelerated senescence of alveolar type II epithelial cells drives pulmonary fibrosis induced by single-walled carbon nanotubes. J Nanobiotechnology 21: 69, 2023.
5. Ma J, Cai H, Long X, Cheng K, Xu X, Zhang D and Li J: Hyaluronic acid bioinspired polymers for the regulation of cell chondrogenic and osteogenic differentiation. Int J Biol Macromol 161: 1011-1020, 2020.
6. Carton F and Malatesta M: Nanotechnological research for regenerative medicine: The role of hyaluronic acid. Int J Mol Sci 25: 3975, 2024.
7. Collum SD, Chen NY, Hernandez AM, Hanmandlu A, Sweeney H, Mertens TCJ, Weng T, Luo F, Molina JG, Davies J, *et al*: Inhibition of hyaluronan synthesis attenuates pulmonary hypertension associated with lung fibrosis. Br J Pharmacol 174: 3284-3301, 2017.
8. Bjermer L, Lundgren R and Hällgren R: Hyaluronan and type III procollagen peptide concentrations in bronchoalveolar lavage fluid in idiopathic pulmonary fibrosis. Thorax 44: 126-131, 1989.
9. Yao ZY, Gong JS, Liu YR, Jiang JY, Zhang YS, Su C, Li H, Kang CL, Liu L, Xu ZH and Shi JS: Genetic variation reveals the enhanced microbial hyaluronan biosynthesis via atmospheric and room temperature plasma. Carbohydr Polym 312: 120809, 2023.
10. Bart G, Vico NO, Hassinen A, Pujol FM, Deen AJ, Ruusala A, Tammi RH, Squire A, Heldin P, Kellokumpu S and Tammi MI: Fluorescence resonance energy transfer (FRET) and proximity ligation assays reveal functionally relevant homo- and heteromeric complexes among hyaluronan synthases HAS1, HAS2, and HAS3. J Biol Chem 290: 11479-11490, 2015.
11. Yang J, Wang L, Zhang Z, Sun Q and Zhang Y: Downregulation of HAS-2 regulates the chondrocyte cytoskeleton and induces cartilage degeneration by activating the RhoA/ROCK signaling pathway. Int J Mol Med 52: 57, 2023.
12. Ge Z, Chen Y, Ma L, Hu F and Xie L: Macrophage polarization and its impact on idiopathic pulmonary fibrosis. Front Immunol 15: 1444964, 2024.
13. Barrett T, Wilhite SE, Ledoux P, Evangelista C, Kim IF, Tomashevsky M, Marshall KA, Phillippy KH, Sherman PM, Holko M, *et al*: NCBI GEO: Archive for functional genomics data sets-update. Nucleic Acids Res 41 (Database Issue): D991-D995, 2013.
14. Cecchini MJ, Hosein K, Howlett CJ, Joseph M and Mura M: Comprehensive gene expression profiling identifies distinct and overlapping transcriptional profiles in non-specific interstitial pneumonia and idiopathic pulmonary fibrosis. Respir Res 19: 153, 2018.
15. Li H, Zhao C, Muhetaer G, Guo L, Yao K, Zhang G, Ji Y, Xing S, Zhou J and Huang X: Integrated RNA-sequencing and network pharmacology approach reveals the protection of Yiqi Huoxue formula against idiopathic pulmonary fibrosis by interfering with core transcription factors. Phytomedicine 104: 154301, 2022.
16. Love MI, Huber W and Anders S: Moderated estimation of fold change and dispersion for RNA-seq data with DESeq2. Genome Biol 15: 550, 2014.
17. Martin M: Cutadapt removes adapter sequences from high-throughput sequencing reads. EMBnet J 17: 10-12, 2011.
18. Dobin A, Davis CA, Schlesinger F, Drenkow J, Zaleski C, Jha S, Batut P, Chaisson M and Gingeras TR: STAR: Ultrafast universal RNA-seq aligner. Bioinformatics 29: 15-21, 2013.
19. Liao Y, Smyth GK and Shi W: featureCounts: An efficient general purpose program for assigning sequence reads to genomic features. Bioinformatics 30: 923-930, 2014.
20. Wolf FA, Angerer P and Theis FJ: SCANPY: Large-scale single-cell gene expression data analysis. Genome Biol 19: 15, 2018.
21. Wolock SL, Lopez R and Klein AM: Scrublet: Computational identification of cell doublets in single-cell transcriptomic data. Cell Syst 8: 281-291.e9, 2019.
22. Satija R, Farrell JA, Gennert D, Schier AF and Regev A: Spatial reconstruction of single-cell gene expression data. Nat Biotechnol 33: 495-502, 2015.
23. Livak KJ and Schmittgen TD: Analysis of relative gene expression data using real-time quantitative PCR and the 2(-Delta Delta C(T)) method. Methods 25: 402-408, 2001.
24. Fuentes-Mateos R, Santos E and Fernández-Medarde A: Optimized protocol for isolation and culture of murine neonatal primary lung fibroblasts. Methods Protoc 6: 14, 2023.
25. Liang J, Jiang D, Jung Y, Xie T, Ingram J, Church T, Degan S, Leonard M, Kraft M and Noble PW: Role of hyaluronan and hyaluronan-binding proteins in human asthma. J Allergy Clin Immunol 128: 403-411.e3, 2011.
26. Fleming J, Magana P, Nair S, Tsenkov M, Bertoni D, Pidruchna I, Lima Afonso MQ, Midlik A, Paramval U, Žídek A, *et al*: AlphaFold protein structure database and 3D-beacons: New data and capabilities. J Mol Biol 437: 168967, 2025.
27. Hess B: P-LINCS: A parallel linear constraint solver for molecular simulation. J Chem Theory Comput 4: 116-122, 2008.
28. Humphrey W, Dalke A and Schulten K: VMD: Visual molecular dynamics. J Mol Graph 14: 33-38, 27-28, 1996.
29. Rosignoli S and Paiardini A: Boosting the full potential of PyMOL with structural biology plugins. Biomolecules 12: 1764, 2022.
30. Moberly JG, Bernards MT and Waynant KV: Key features and updates for origin 2018. J Cheminform 10: 5, 2018.
31. Kumari R, Kumar R; Open Source Drug Discovery Consortium and Lynn A: g_mmpbsa-a GROMACS tool for high-throughput MM-PBSA calculations. J Chem Inf Model 54: 1951-1962, 2014.
32. Martinez Molina D, Jafari R, Ignatushchenko M, Seki T, Larsson EA, Dan C, Sreekumar L, Cao Y and Nordlund P: Monitoring drug target engagement in cells and tissues using the cellular thermal shift assay. Science 341: 84-87, 2013.
33. Tan BX, Brown CJ, Ferrer FJ, Yuen TY, Quah ST, Chan BH, Jansson AE, Teo HL, Nordlund P and Lane DP: Assessing the efficacy of Mdm2/Mdm4-inhibiting stapled peptides using cellular thermal shift assays. Sci Rep 5: 12116, 2015.
34. Selman M and Pardo A: Pathogenic mechanisms in the development of diffuse pulmonary fibrosis. Braz J Med Biol Res 29: 1117-1126, 1996.
35. Rosser JI, Nagy N, Goel R, Kaber G, Demirdjian S, Saxena J, Bollyky JB, Frymoyer AR, Pacheco-Navarro AE, Burgener EB, *et al*: Oral hymecromone decreases hyaluronan in human study participants. J Clin Invest 132: e157983, 2022.
36. Ghatak S, Markwald RR, Hascall VC, Dowling W, Lottes RG, Baatz JE, Beeson G, Beeson CC, Perrella MA, Thannickal VJ and Misra S: Transforming growth factor β1 (TGFβ1) regulates CD44V6 expression and activity through extracellular signal-regulated kinase (ERK)-induced EGR1 in pulmonary fibrogenic fibroblasts. J Biol Chem 292: 10465-10489, 2017.
37. Qin W, Spek CA, Scicluna BP, van der Poll T and Duitman J: Myeloid DNA methyltransferase3b deficiency aggravates pulmonary fibrosis by enhancing profibrotic macrophage activation. Respir Res 23: 162, 2022.
38. Liu L, Wu P, Wei Y, Lu M, Ge H, Wang P, Sun J, Horng T, Liu X, Shen X, *et al*: TWEAK-Fn14 signaling protects mice from pulmonary fibrosis by inhibiting fibroblast activation and recruiting pro-regenerative macrophages. Cell Rep 44: 115220, 2025.
39. Zhou JW, Bai Y, Guo JQ, Li YY, Liu YF, Liang C, Xing YR, Guo HL, Qi TX, Wu J and Hu D: Peroxiredoxin 4 as a switch regulating PTEN/AKT axis in alveolar macrophages activation. Signal Transduct Target Ther 10: 352, 2025.
40. Li S, Xu H, Liu S, Hou J, Han Y, Li C, Li Y, Zheng G, Wei Z, Yang F, *et al*: Targeting Lp-PLA2 inhibits profibrotic monocyte-derived macrophages in silicosis through restoring cardiolipin-mediated mitophagy. Cell Mol Immunol 22: 776-790, 2025.

41. Kultti A, Pasonen-Seppänen S, Jauhiainen M, Rilla KJ, Kärnä R, Pyöriä E, Tammi RH and Tammi MI: 4-Methylumbelliferone inhibits hyaluronan synthesis by depletion of cellular UDP-glucuronic acid and downregulation of hyaluronan synthase 2 and 3. Exp Cell Res 315: 1914-1923, 2009.
42. He XY, Zhao WL, Yao LP, Sun P, Cheng G, Liu YL, Yu Y, Liu Y, Wang TJ, Zhang QY, *et al*: Orcinol glucoside targeted p38 as an agonist to promote osteogenesis and protect glucocorticoid-induced osteoporosis. Phytomedicine 119: 154953, 2023.
43. Li J, He P, Zhang J and Li N: Orcinol glucoside improves the depressive-like behaviors of perimenopausal depression mice through modulating activity of hypothalamic-pituitary-adrenal/ovary axis and activating BDNF-TrkB-CREB signaling pathway. Phytother Res 35: 5795-5807, 2021.
44. Wang X, Li G, Li P, Huang L, Huang J and Zhai H: Anxiolytic effects of orcinol glucoside and orcinol monohydrate in mice. Pharm Biol 53: 876-881, 2015.
45. Nahak P, Gajbhiye RL, Karmakar G, Guha P, Roy B, Besra SE, Bikov AG, Akentiev AV, Noskov BA, Nag K, *et al*: Orcinol glucoside loaded polymer-lipid hybrid nanostructured lipid carriers: potential cytotoxic agents against gastric, colon and hepatoma carcinoma cell lines. Pharm Res 35: 198, 2018.
46. Nie Y, Dong X, He Y, Yuan T, Han T, Rahman K, Qin L and Zhang Q: Medicinal plants of genus Curculigo: Traditional uses and a phytochemical and ethnopharmacological review. J Ethnopharmacol 147: 547-563, 2013.
47. Yang YM, Noureddin M, Liu C, Ohashi K, Kim SY, Ramnath D, Powell EE, Sweet MJ, Roh YS, Hsin IF, *et al*: Hyaluronan synthase 2-mediated hyaluronan production mediates Notch1 activation and liver fibrosis. Sci Transl Med 11: eaat9284, 2019.
48. Klee S, Picart-Armada S, Wenger K, Birk G, Quast K, Veyel D, Rist W, Violet C, Luippold A, Haslinger C, *et al*: Transcriptomic and proteomic profiling of young and old mice in the bleomycin model reveals high similarity. Am J Physiol Lung Cell Mol Physiol 324: L245-L258, 2023.